

Article

Excitation Signal Design for Fast Electrochemical Impedance Spectroscopy in Battery Testing

Sneha Sundaresan ¹, Krishna R. Pattipati ² and Balakumar Balasingam ^{1,*}¹ Department of Electrical and Computer Engineering, University of Windsor, 401 Sunset Ave., Windsor, ON N9B 3P4, Canada; sundare1@uwindsor.ca² Department of Electrical and Computer Engineering, University of Connecticut, 371 Fairfield Way, Storrs, CT 06269, USA; krishna.pattipati@uconn.edu

* Correspondence: singam@uwindsor.ca; Tel.: +1-(519)-253-3000

Abstract

Electrochemical impedance spectroscopy (EIS) is a widely used technique for analyzing battery dynamics over a broad frequency spectrum. Conventional state-of-the-art EIS methods involve applying a sequence of sinusoidal excitation signals, ranging from very low to very high frequencies, to capture the impedance response of the battery. However, this process is time-consuming, often requiring several hours to complete. Alternatively, approaches using pulse-based excitation have shown promise in reducing test time but often suffer from challenges in handling measurement noise and poor frequency resolution, especially at low frequencies. This work presents an improved rectangular pulse-based impedance characterization technique that enhances low-frequency resolution, increases robustness to noise, and reduces experimental time. This is accomplished through the following three key contributions of this paper: First, it establishes statistical noise properties in the Fourier-transformed signals, enabling effective noise reduction through averaging. Second, it proposes a log-frequency clustering approach to average impedance data, enhancing the accuracy of the impedance spectrum. Third, it presents a systematic pulse design method using the knowledge of the approximate time constants of the system to select the sampling interval, pulse width, and rest duration for reduced test time, improved low-frequency resolution, and enhanced signal-to-noise ratio (SNR). Together, the proposed approach enables faster and more accurate impedance characterization. Simulation analysis and experimental results confirm that the proposed approach enhances spectral resolution at low frequencies, mitigates the impact of noise at high frequencies, and significantly improves the reliability of impedance estimates at a faster measurement time frame.



Academic Editor: Sylvain Franger

Received: 16 September 2025

Revised: 28 October 2025

Accepted: 3 November 2025

Published: 5 November 2025

Citation: Sundaresan, S.; Pattipati, K.R.; Balasingam, B. Excitation Signal Design for Fast Electrochemical Impedance Spectroscopy in Battery Testing. *Batteries* **2025**, *11*, 408. <https://doi.org/10.3390/batteries11110408>

Copyright: © 2025 by the authors. Licensee MDPI, Basel, Switzerland. This article is an open access article distributed under the terms and conditions of the Creative Commons Attribution (CC BY) license (<https://creativecommons.org/licenses/by/4.0/>).

Keywords: battery management systems; electrochemical impedance spectroscopy; battery testing; impedance analysis; state of health

1. Introduction

Electrochemical impedance spectroscopy (EIS) is a well-established method for analyzing the dynamic behavior of electrochemical systems, including batteries [1–3]. The impedance parameters derived from EIS play a central role in estimating key battery states such as state of charge (SOC) [4,5], state of health (SOH) [6–10], and remaining useful life (RUL). Leveraging EIS within battery management systems (BMSs) enables accurate battery state estimation that improves its performance, safety, and reliability in applications, such as electric vehicles (EVs) and energy storage systems.

1.1. Literature Review

State-of-the-art EIS techniques involve applying small-amplitude sinusoidal current signals at multiple discrete frequencies, typically spanning from low to high, and measuring the resulting voltage to construct the impedance spectrum [11–13]. While effective, this approach is inherently time-consuming, especially at low frequencies, which limits its practical utility in real-time applications. To address this limitation, pulse-based excitation methods have gained attention due to their ability to significantly shorten the measurement time while still enabling accurate impedance estimation [14–21]. Unlike sinusoidal excitation, which captures information at a single frequency and requires sequential sweeps, pulse excitation excites a broad range of frequency components at once, making it a more efficient alternative. By applying a fast Fourier transform (FFT) [22] to the input current and the concomitant voltage response, the impedance spectrum can be derived, enabling analysis in the frequency domain.

Early pulse-based studies explored a range of time-domain excitations. For instance, in [23], a voltage step signal was utilized as the excitation source for impedance analysis, while the authors in [24] extended this approach using both step and pulse current signals. In both studies, the impedance spectrum was derived by applying the Laplace transform to the input and output signals. Building on these foundations, a novel method was proposed in [25] to extract the impedance spectrum directly from the pulse charge/discharge curves of batteries, offering an alternative approach to traditional EIS techniques. In [26], a rapid computation method for broadband battery impedance utilizing the S-transform and employing Gaussian window was introduced. Furthermore, wavelet transform-based methods were explored in [27–29], where pulse current and voltage signals were analyzed in the time–frequency domain to extract the impedance information, highlighting the potential of wavelet analysis for EIS. In a broader comparison, authors in [30] investigated various excitation signals, including rectangular pulses, Gaussian inputs, and sinc waveforms, and compared their resulting impedance spectra against those obtained through standard sinusoidal excitation.

In parallel with advances in EIS techniques, several recent studies have explored online or embedded impedance measurement methods that can operate directly within the BMS. In [31], an embedded EIS platform capable of measuring impedance while the cell was charging or discharging was developed that demonstrated the feasibility of continuous *in situ* monitoring. Perturbation-based impedance characterization approaches and the challenges of integrating accurate yet low-cost impedance sensing in on-board BMS hardware were discussed in [32]. The authors in [33] used operational current–voltage data from the battery for online estimation of the impedance spectrum and RUL. Similarly, Ref. [34] presented a single-perturbation-cycle method that estimates impedance in real time through closed-loop converter control, while [35] introduced a low-power integrated sensing and parametric modeling approach for online EIS. More recently, Ref. [36] employed data-driven reconstruction of impedance spectra from early-stage relaxation curves, further advancing online diagnostic capabilities. Collectively, these studies highlight the growing trend toward real-time, embedded impedance diagnostics that minimize test duration and hardware complexity. Building upon this direction, the present work develops a pulse-based discrete-frequency framework that is analytically tractable, fast, and directly extendable to online BMS implementation. Table 1 summarizes the key references in Section 1, highlighting the type of excitation signal used and the underlying design principle, processing domain, and corresponding testing outcomes.

Table 1. Summary of excitation signal design principles in prior EIS studies.

References	Excitation Signal	Principle of Design	Processing Technique	Measurement Time	Testing Outcomes
[11–13]	Sinusoidal (frequency sweep)	Single-frequency perturbation ensuring linearity; one frequency at a time	FFT	≈90 min	High accuracy and noise robustness; unsuitable for online use due to long duration
[23]	Voltage step	Step perturbation producing broadband frequency content via transient response	FFT	≈60 min	Captures impedance over a wide band in a single step; can exhibit nonlinearity at high amplitudes
[24]	Current step and pulse	Pulse with defined ON and OFF durations; excites multiple frequencies simultaneously	FFT	Several minutes	Enables broadband estimation; sensitive to SNR
[25]	Charge–discharge curves of battery	Battery parameters are calculated to construct the impedance spectrum	Distribution of relaxation time (DRT) analysis	Order of seconds	Suitable for BMS implementation
[26–29]	Time–frequency signals	Small-step current with optimized parameters	Complex Morlet wavelet transform	Order of seconds	Useful under dynamic load conditions
[30]	Gaussian, sinc, and rectangular pulses	Comparative study of waveform types balancing spectral coverage and energy distribution	FFT	1–2 min	Optimizes trade-off between broadband energy and spectral accuracy
[31–36]	Online perturbations	Small-signal or adaptive pulses injected during operation; low amplitude to avoid system disruption	Real-time digital signal processing (DSP)	Order of seconds	Enables online or in situ impedance monitoring; compatible with EV or BMS integration

1.2. Research Gap and Motivation

Although pulse-based methods have demonstrated strong potential as faster and more efficient alternatives to conventional EIS, several critical challenges remain unaddressed in the literature. A primary limitation lies in the sensitivity to noise, particularly in the high-frequency region where the signal-to-noise ratio (SNR) tends to degrade. This often results in unreliable impedance estimates when compared with sinusoidal excitation. While studies such as [11,12] have systematically analyzed noise effects in sinusoidal-based EIS, equivalent investigations for pulse-based approaches are sparse. As a result, the robustness of pulse excitation under realistic measurement conditions remains insufficiently understood.

Another important gap concerns the systematic selection of pulse design parameters, including sampling frequency, pulse duration, and relaxation period, which directly determine the spectral content and resolution of the resulting impedance. Existing works on step or pulse excitations [23–25] demonstrate feasibility but provide little methodological guidance on parameter tuning for accurate and reliable impedance estimation across the full frequency range. In particular, the low-frequency region suffers from limited resolution, and improper choice of excitation parameters can further compromise accuracy.

Moreover, while alternative signal processing methods such as wavelet transforms [27–29] and generalized excitation signal comparisons [30] have been explored, there is still no

unified framework linking pulse signal design, noise robustness, and impedance estimation accuracy.

By systematically analyzing the interplay of noise, excitation parameters, and spectral resolution, this work aims to establish clear methodological guidelines for pulse-based impedance estimation, thereby enabling faster, more robust, and accurate characterization of batteries in real-world settings.

1.3. Contributions

The key contributions of this paper are outlined below:

1. Statistical analysis of the noise characteristics: The first major contribution of this work is the analytical derivation of the statistical property, i.e., the mean of the Fourier-transformed voltage noise, current noise, and resulting impedance noise. This paper mathematically shows that the voltage and current measurement noises retain their zero-mean property in the frequency domain. This property enables effective noise reduction in the raw impedance estimates through averaging, leading to a significant improvement in the accuracy of the impedance spectrum.
2. Zero-padding approach to improve resolution: The impedance spectrum derived from the proposed rectangular pulse excitation exhibits a non-uniform distribution of impedance estimates across the frequency range. There is a higher concentration of estimates in the high-frequency region and fewer in the low-frequency region. To enhance the resolution in the low-frequency domain, a zero-padding technique is introduced.
3. Log-scaled frequency clustering for improved spectral representation: To address the imbalance in the number of measurements across different frequencies, a log-scale clustering strategy is proposed. By grouping impedance values into logarithmically spaced frequency bins and averaging within each bin, a more uniform and noise-reduced spectral representation is obtained across the frequency ranges.
4. Time-constant-informed rectangular pulse design for accurate characterization: This paper also introduces a systematic method for designing rectangular pulse excitation signals based on the knowledge of the approximate time constants of the system. It offers practical recommendations for selecting the sampling interval, pulse width, and zero-current duration, with the goal of reducing the experimental time, enhancing the low-frequency spectral resolution, and improving the SNR.

1.4. Organization of the Paper

The remainder of this paper is organized into the following sections: Section 2 introduces the rectangular pulse excitation signal and its transformation in the frequency domain using Fourier transform. Statistical analysis of the impedance noise is performed in Section 3. Section 4 discusses the design of the excitation signal for improved SNR. Simulation analyses are provided in Section 5, whereas the experimental procedures and results are detailed in Section 6. The paper is concluded in Section 7.

2. Rectangular Pulse Excitation Signal

This section discusses the characterization of the electrochemical impedance behavior of lithium-ion batteries using a rectangular pulse excitation signal. Figure 1 shows a rectangular excitation current signal (in blue) and typical battery response (in red). The current pulse has an amplitude of $-a$ applied for an ON duration, T_{on} , followed by a zero-current rest period extending to the total duration, T_{total} .

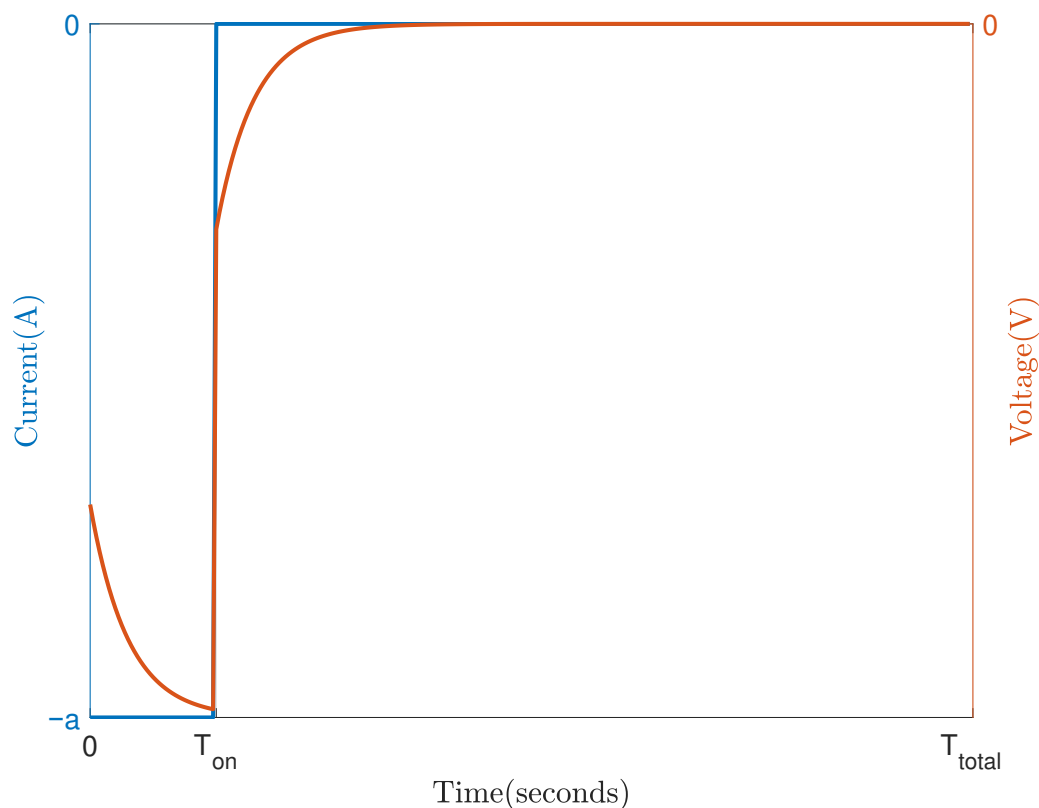


Figure 1. Rectangular pulse current excitation (blue) and concomitant voltage response (red).

The equivalent circuit model (ECM) of the battery shown in Figure 2 represents a generalized lithium-ion cell, applicable to a wide range of intercalation-type chemistries including nickel–manganese–cobalt oxide (NMC), lithium cobalt oxide (LCO) [37], lithium manganese oxide (LMO) [38], lithium iron phosphate (LFP) [39,40], and lithium titanate oxide (LTO). The ECM comprises (i) a voltage source in open-circuit condition, $E[k]$; (ii) ohmic resistance, R_0 ; (iii) two RC circuits with RC pairs (R_1, C_1) , and (R_2, C_2) ; and (iv) a Warburg impedance element, Z_W , to capture low-frequency diffusion effects. This configuration has been extensively adopted in the literature to characterize lithium-ion cell impedance behavior under both traditional EIS and pulse-based excitation methods [3,15,17,18,41]. Using the widely accepted ECM in Figure 2, this work will demonstrate that the impedance spectrum can be obtained rapidly from the proposed short pulse excitation signal, enabling faster battery testing compared to traditional EIS methods. The selected model provides sufficient fidelity for analyzing pulse-based impedance response while maintaining simplicity for online estimation and real-time BMS implementation, making it well suited for both algorithm design and experimental testing.

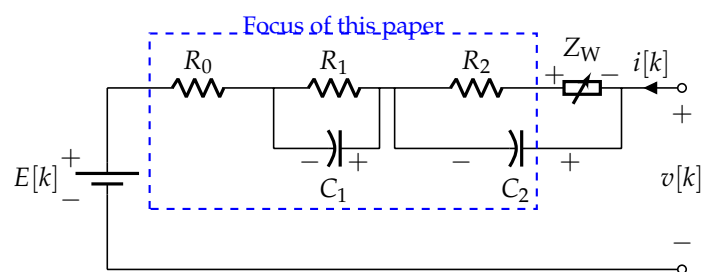


Figure 2. Equivalent circuit model (ECM) of a lithium-ion cell, consisting of an open-circuit voltage source $E[k]$, ohmic resistance R_0 , two RC branches (R_1, C_1) and (R_2, C_2) , and a Warburg diffusion element Z_W , representing low-frequency diffusion. The blue dashed box indicates the subsystem analyzed in this paper for pulse-based impedance characterization.

The voltage response of the battery, denoted as $v[k]$, corresponds to the input current, $i[k]$, shown in Figure 2. While $i[k]$ and $v[k]$ represent the system behavior in the time domain, impedance is defined in the frequency domain. To obtain the frequency-domain representation, the discrete Fourier transforms (DFTs) of $i[k]$ and $v[k]$ are first computed to determine their spectral characteristics, and the resulting voltage and current spectra are then used to calculate the discrete-frequency impedance response.

The rectangular pulse excitation signal shown in Figure 1 can be discretized by sampling at intervals of ' t_s ' seconds. Let ' K ' denote the number of samples in the 'ON' duration of the pulse, i.e., $K = \frac{T_{on}}{t_s}$, and ' N ' denote the total number of samples in the signal, i.e., $N = \frac{T_{total}}{t_s}$. The discrete rectangular pulse signal, $i[k]$, shown in Figure 3, is defined as

$$i[k] = \begin{cases} -a, & k = 0, 1, 2, \dots, (K-1) \\ 0, & k = K, K+1, \dots, (N-1) \end{cases} \quad (1)$$

For DFT, the continuous frequency ' ω ' of the transform is discretised to ' N ' frequency bins as

$$\omega_m = \left(\frac{2\pi f_s}{N} \right) m, \quad m = 0, 1, \dots, N-1 \quad (2)$$

where $f_s = \frac{1}{t_s}$ is the sampling frequency and $\Delta f = \frac{f_s}{N}$ is the frequency resolution of the transform, which denotes the spacing between ' m ' frequency bins in the DFT.

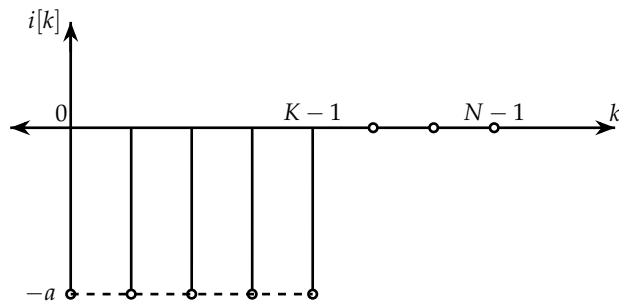


Figure 3. Discretized rectangular pulse excitation signal comprising ' K ' ON samples and ' $N-K$ ' OFF samples.

The DFT of the discrete current signal, $i[k]$, which is a vector of input current values, is given by,

$$I(m) = \sum_{k=0}^{N-1} i[k] e^{-jm(\frac{2\pi}{N})k}, \quad m = 0, 1, \dots, N-1 \quad (3)$$

Refer to Appendix A for the details of this transformation, which can be written as $I(0) = -aK$ for $m = 0$, and

$$I(m) = -ae^{-jm\frac{\pi}{N}(K-1)} \left(\frac{\sin(\frac{mK\pi}{N})}{\sin(\frac{m\pi}{N})} \right), \quad m = 1, \dots, N-1 \quad (4)$$

The DFT of the response, $v[k]$, is given by,

$$V(m) = \sum_{k=0}^{N-1} v[k] e^{-jm(\frac{2\pi}{N})k}, \quad m = 0, 1, \dots, N-1 \quad (5)$$

Then, the impedance in the m^{th} frequency bin is given by

$$Z(m) = \frac{V(m)}{I(m)} \quad (6)$$

In (6), the impedance in each discrete frequency bin is defined as the ratio of the DFT-transformed voltage and current signals. The complex-valued impedance, $Z(m)$, encapsulates both resistive and reactive behavior at each frequency, and its components are typically visualized through Nyquist plots. To illustrate the characteristic impedance response of a lithium-ion cell modeled by the ECM in Figure 2, Figure 4 presents a representative Nyquist plot. The Nyquist plot captures the characteristic semicircular arcs and diffusive tail associated with different electrochemical processes. The intercept at R_0 corresponds to the ohmic resistance, while the subsequent arcs reflect the solid electrolyte interface (SEI) and charge-transfer (CT) and double-layer (DL) effects modeled by the (R_1, C_1) and (R_2, C_2) branches, respectively. At very low frequencies, the 45° line, which is the Warburg impedance, indicates the diffusion process within the battery. Together, these features highlight the distinct resistive and capacitive contributions governing the battery's dynamic behavior.

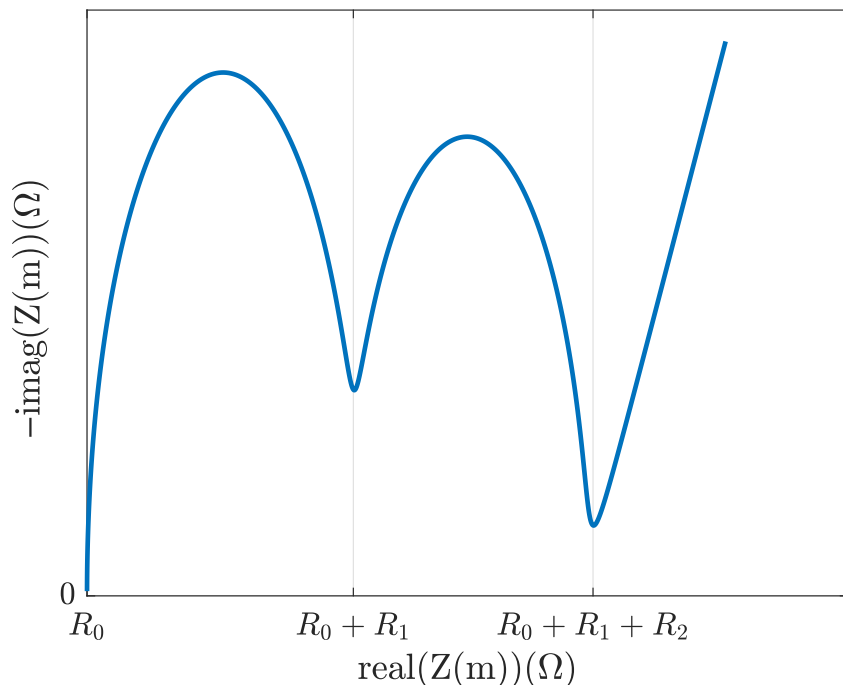


Figure 4. Typical Nyquist plot of a battery showing the ohmic resistance, R_0 ; SEI and CT resistances, R_1 and R_2 ; and the Warburg diffusion tail at low frequencies.

3. Mean of the Impedance Noise

This section presents statistical analysis of impedance noise. Let us denote the measured voltage from the battery in vector format as

$$\mathbf{z}_v = \mathbf{v} + \mathbf{n}_v \quad (7)$$

where \mathbf{v} is the true voltage signal and \mathbf{n}_v is the voltage noise vector.

The DFT of the measured voltage, \mathbf{z}_v , can be written as

$$\check{\mathbf{z}}_v = \mathbf{F}\mathbf{z}_v = \mathbf{F}(\mathbf{v} + \mathbf{n}_v) = \check{\mathbf{v}} + \check{\mathbf{n}}_v \quad (8)$$

where $\mathbf{F} \in \mathbb{C}^{N \times N}$ is the unitary DFT matrix given by

$$\mathbf{F}_{m,k} = e^{-jm\frac{2\pi}{N}k}, \quad m, k = 0, \dots, N-1, \quad (9)$$

and $\check{\mathbf{v}} \in \mathbb{C}^{N \times 1}$ and $\check{\mathbf{n}}_v \in \mathbb{C}^{N \times 1}$ are given by

$$\begin{aligned}\check{\mathbf{v}} &= \mathbf{F}\mathbf{v}, && \text{(DFT of the true voltage signal)} \\ \check{\mathbf{n}}_v &= \mathbf{F}\mathbf{n}_v, && \text{(DFT of the voltage noise)}\end{aligned}\quad (10)$$

Similarly, the DFT of the input current \mathbf{z}_i can be written as

$$\check{\mathbf{z}}_i = \mathbf{F}\mathbf{z}_i = \mathbf{F}(\mathbf{i} + \mathbf{n}_i) = \check{\mathbf{i}} + \check{\mathbf{n}}_i \quad (11)$$

where $\check{\mathbf{i}} \in \mathbb{C}^{N \times 1}$ and $\check{\mathbf{n}}_i \in \mathbb{C}^{N \times 1}$ are given by

$$\begin{aligned}\check{\mathbf{i}} &= \mathbf{F}\mathbf{i}, && \text{(DFT of the true current signal)} \\ \check{\mathbf{n}}_i &= \mathbf{F}\mathbf{n}_i, && \text{(DFT of the current noise)}\end{aligned}\quad (12)$$

See Appendix B for details on how the zero-mean property of voltage and current noise is preserved in the frequency domain.

Let us now consider the impedance at the m^{th} frequency bin

$$Z(m) = \frac{\mathbf{f}_m \mathbf{z}_v}{\mathbf{f}_m \mathbf{z}_i} = \frac{\mathbf{f}_m \mathbf{v} + \mathbf{f}_m \mathbf{n}_v}{\mathbf{f}_m \mathbf{i} + \mathbf{f}_m \mathbf{n}_i} = \frac{\mathbf{a}^T \mathbf{z}_v}{\mathbf{a}^T \mathbf{z}_i} = \frac{\mathbf{a}^T \mathbf{v} + \mathbf{a}^T \mathbf{n}_v}{\mathbf{a}^T \mathbf{i} + \mathbf{a}^T \mathbf{n}_i} \quad (13)$$

where \mathbf{f}_m is the m^{th} row of \mathbf{F} which is denoted for simplicity as

$$\mathbf{a}^T = \mathbf{f}_m \quad (14)$$

By recognizing that $\mathbf{a} \in \mathbb{C}^{N \times 1}$, let us decompose it into its real and complex parts as

$$\mathbf{a} = \mathbf{a}_r + j\mathbf{a}_i \quad (15)$$

Now, $Z(m)$ can be written as

$$Z(m) = \frac{(\mathbf{a}_r + j\mathbf{a}_i)^T \mathbf{v} + (\mathbf{a}_r + j\mathbf{a}_i)^T \mathbf{n}_v}{(\mathbf{a}_r + j\mathbf{a}_i)^T \mathbf{i} + (\mathbf{a}_r + j\mathbf{a}_i)^T \mathbf{n}_i} \quad (16)$$

$$= \frac{(\mathbf{a}_r^T \mathbf{v} + \mathbf{a}_r^T \mathbf{n}_v) + j(\mathbf{a}_i^T \mathbf{v} + \mathbf{a}_i^T \mathbf{n}_v)}{(\mathbf{a}_r^T \mathbf{i} + \mathbf{a}_r^T \mathbf{n}_i) + j(\mathbf{a}_i^T \mathbf{i} + \mathbf{a}_i^T \mathbf{n}_i)} \quad (17)$$

$$= Z_r(m) + jZ_i(m) \quad (18)$$

where $Z_r(m)$ and $Z_i(m)$ are the real and imaginary parts, respectively, of the impedance. This can be further written according to the signal and noise portions as follows:

$$Z_r(m) = S_r(m) + N_r(m) \quad (19)$$

$$Z_i(m) = S_i(m) + N_i(m) \quad (20)$$

where

$$S_r(m) = \frac{(\mathbf{a}_r^T \mathbf{v})(\mathbf{a}_r^T \mathbf{i}) + (\mathbf{a}_i^T \mathbf{v})(\mathbf{a}_i^T \mathbf{i})}{(\mathbf{a}_r^T \mathbf{i} + \mathbf{a}_r^T \mathbf{n}_i)^2 + (\mathbf{a}_i^T \mathbf{i} + \mathbf{a}_i^T \mathbf{n}_i)^2} \quad (21)$$

$$S_i(m) = \frac{(\mathbf{a}_r^T \mathbf{i})(\mathbf{a}_i^T \mathbf{v}) - (\mathbf{a}_i^T \mathbf{v})(\mathbf{a}_r^T \mathbf{i})}{(\mathbf{a}_r^T \mathbf{i} + \mathbf{a}_r^T \mathbf{n}_i)^2 + (\mathbf{a}_i^T \mathbf{i} + \mathbf{a}_i^T \mathbf{n}_i)^2}$$

and $N_r(m)$ and $N_i(m)$ are given below.

$$\begin{aligned} N_r(m) &= \frac{(\mathbf{a}_r^T \mathbf{v})(\mathbf{a}_r^T \mathbf{n}_i) + (\mathbf{a}_r^T \mathbf{n}_v)(\mathbf{a}_r^T \mathbf{i}) + (\mathbf{a}_r^T \mathbf{n}_v)(\mathbf{a}_r^T \mathbf{n}_i)}{(\mathbf{a}_r^T \mathbf{i} + \mathbf{a}_r^T \mathbf{n}_i)^2 + (\mathbf{a}_i^T \mathbf{i} + \mathbf{a}_i^T \mathbf{n}_i)^2} \\ &\quad + \frac{(\mathbf{a}_i^T \mathbf{v})(\mathbf{a}_i^T \mathbf{n}_i) + (\mathbf{a}_i^T \mathbf{n}_v)(\mathbf{a}_i^T \mathbf{i}) + (\mathbf{a}_i^T \mathbf{n}_v)(\mathbf{a}_i^T \mathbf{n}_i)}{(\mathbf{a}_i^T \mathbf{i} + \mathbf{a}_i^T \mathbf{n}_i)^2 + (\mathbf{a}_i^T \mathbf{i} + \mathbf{a}_i^T \mathbf{n}_i)^2} \\ N_i(m) &= \frac{(\mathbf{a}_i^T \mathbf{v})(\mathbf{a}_i^T \mathbf{n}_i) + (\mathbf{a}_i^T \mathbf{n}_v)(\mathbf{a}_i^T \mathbf{i}) + (\mathbf{a}_i^T \mathbf{n}_v)(\mathbf{a}_r^T \mathbf{n}_i)}{(\mathbf{a}_r^T \mathbf{i} + \mathbf{a}_r^T \mathbf{n}_i)^2 + (\mathbf{a}_i^T \mathbf{i} + \mathbf{a}_i^T \mathbf{n}_i)^2} \\ &\quad - \frac{(\mathbf{a}_r^T \mathbf{v})(\mathbf{a}_i^T \mathbf{n}_i) + (\mathbf{a}_r^T \mathbf{n}_v)(\mathbf{a}_i^T \mathbf{i}) + (\mathbf{a}_r^T \mathbf{n}_v)(\mathbf{a}_i^T \mathbf{n}_i)}{(\mathbf{a}_i^T \mathbf{i} + \mathbf{a}_i^T \mathbf{n}_i)^2 + (\mathbf{a}_i^T \mathbf{i} + \mathbf{a}_i^T \mathbf{n}_i)^2} \end{aligned}$$

It can be verified that

$$\mathbb{E}[N_r(m)] = 0, \quad \mathbb{E}[N_i(m)] = 0 \quad (22)$$

4. Excitation Signal Design for Improved SNR

4.1. Selection of Sampling Time, t_s

The sampling time should be chosen to accurately capture the system dynamics associated with the smallest time constant [42]. As a rule of thumb, it should be less than one-tenth of the system's minimum time constant, i.e.,

$$t_s \leq \frac{\tau_{min}}{10} \quad (23)$$

For the ECM shown in Figure 2, the system's minimum time constant is determined by the smallest RC product, i.e.,

$$\tau_{min} = \min(R_1 C_1, R_2 C_2) \quad (24)$$

The sampling time condition expressed in (23) serves as a general guideline for discretizing the system dynamics such that the fastest electrochemical processes are adequately resolved. The smallest time constant τ_{min} , representing the fastest dynamic behavior of the cell, can be inferred from previous EIS measurements or from the representative literature data for similar Li-ion chemistries. For example, [43] reports characteristic RC time constants of approximately 0.1 ms for ohmic and SEI processes, 10–50 ms for charge-transfer kinetics in LCO and NMC cells, and several hundred milliseconds for the low-frequency diffusion-dominated behavior in LFP and LTO chemistries. More detailed timescale ranges for a variety of chemistries, together with the corresponding literature sources, are summarized in Table 1 of [43].

Remark 1. There is a trade-off in selecting the sampling time t_s .

1. *Smaller t_s :* The advantage of a smaller t_s is that the high-frequency response of the battery is accurately captured. However, choosing a very small t_s can be challenging to implement in practice.
2. *Larger t_s :* Larger t_s reduces the volume of collected data, lowering the computational load. However, it limits the ability to capture high-frequency impedance features and introduces the risk of aliasing if fast dynamics are present.

4.2. Selection of T_{on}

This section discusses how the minimum T_{on} for the pulse design is determined based on the zero-crossings in the frequency spectrum. The DFT of the current excitation signal is

given in (A5). To determine the points ' m ' where this signal crosses zero, i.e., to find the zero-crossings, we set

$$I(m) = 0 \quad (25)$$

which is

$$-ae^{-jm\frac{\pi}{N}(K-1)} \left(\frac{\sin(\frac{mK\pi}{N})}{\sin(\frac{m\pi}{N})} \right) = 0 \quad (26)$$

The zero-crossings occur when

$$\sin\left(\frac{mK\pi}{N}\right) = 0 \quad (27)$$

This means that

$$\frac{mK\pi}{N} = p\pi \quad (28)$$

where p is an integer. Then,

$$m = p\frac{N}{K} = p\frac{1}{D} \quad (29)$$

where $D = K/N$ is the duty cycle of the pulse. This implies that the zero-crossings of the excitation signal's spectrum occur at integer multiples of $\frac{N}{K}$, or equivalently, at integer multiples of $\frac{1}{D}$. The total number of zero-crossings, N_z , within $\frac{N}{2}$ frequency bins—equivalent to $\frac{f_s}{2}$ —is

$$N_z = \frac{\frac{N}{2}}{\frac{1}{D}} = \frac{K}{2} \quad (30)$$

The lowest T_{on} corresponds to a rectangular pulse whose total number of zero-crossings, N_z , is minimized. In this design, the main lobe of the spectrum will exclusively span all frequencies of interest up to the system's maximum frequency, corresponding to $\frac{f_s}{2}$. This requires that the first and only zero-crossing of the spectrum occurs at

$$m = \frac{1}{D} \quad (31)$$

In terms of frequency, (31) translates to $\frac{1}{D} \left(\frac{f_s}{N} \right)$, which crosses zero at $\frac{f_s}{2}$, i.e.,

$$\frac{1}{D} \left(\frac{f_s}{N} \right) = \frac{f_s}{2} \quad (32)$$

Solving this yields

$$K = 2, \text{ i.e.,} \quad (33)$$

$$T_{on} = 2t_s \quad (34)$$

Based on the criteria for sampling time in (23), the criteria for minimum T_{on} in (34) can be written as

$$(T_{on})_{min} = \frac{\tau_{min}}{5} \quad (35)$$

Thus, T_{on} for the pulse design can be chosen as

$$T_{on} \geq \frac{\tau_{min}}{5} \quad (36)$$

Remark 2. There is a trade-off in selecting the pulse duration T_{on} .

1. *Smaller T_{on} :* The advantage of a smaller T_{on} is that it reduces the number of zero-crossings in the excitation spectrum. A smaller T_{on} ensures that the amplitudes of the main and side lobes remain relatively close, which means that the excitation amplitude stays nearly constant across all frequencies. Another advantage of a smaller T_{on} is that it reduces the total experiment time. Finally, smaller T_{on} reduces the effect to the OCV during the experiment, thereby ensuring that the battery's operating condition is not significantly altered during the experiment.
2. *Larger T_{on} :* Larger T_{on} leads to a significantly larger main lobe amplitude in the excitation spectrum. Since zero-crossings occur at integer multiples of $1/D$, a higher duty cycle results in a narrower main lobe, concentrating more energy at low frequencies. This characteristic is particularly advantageous for accurately estimating the low-frequency resistance of the battery.

4.3. Selection of T_{off}

With T_{on} set, the zero-current duration of the excitation signal, T_{off} , can be chosen to be at least ten times the system's largest time constant, i.e.,

$$T_{off} \geq 10\tau_{max} \quad (37)$$

which provides sufficient time for the dynamics of the system to settle. The total duration of the excitation signal, T_{total} , is given by

$$T_{total} = T_{on} + T_{off} \quad (38)$$

where T_{on} and T_{off} are determined based on the system's time constants.

4.4. Zero-Padding

In [44], T_{total} was chosen to achieve a desired frequency resolution for the DFT. In this paper, its selection is refined based on the knowledge of the system's time constants. To further improve low-frequency resolution, zero-padding is applied by appending zeros to the time-domain signal prior to the DFT, increasing the number of frequency bins and reducing their spacing. This enhances low-frequency detail in the impedance spectrum without increasing the actual experiment duration.

5. Simulation Analysis

This section presents the analysis of pulse-based EIS through simulations conducted in MATLAB R2021b. In this paper, it is assumed that $E[k] = 0$ to eliminate any bias effects caused by the OCV. The following parameters of the ECM are used in the simulations: $R_0 = 0.5 \Omega$, $R_1 = 0.6 \Omega$, $C_1 = 5F$, $R_2 = 0.7 \Omega$, and $C_2 = 0.05F$, and diffusion effects are assumed to be zero. The impedance for the ECM depicted in Figure 2 is theoretically expressed as

$$Z_t(m) = R_0 + \frac{R_1}{1 + j(2\pi f_m)R_1C_1} + \frac{R_2}{1 + j(2\pi f_m)R_2C_2} \quad (39)$$

where f_m denotes the m^{th} frequency bin of DFT, where Z_t is evaluated. Figure 5a shows the theoretical impedance spectrum, i.e., the magnitude of impedance versus frequency for a range of frequencies between 0 Hz and 1000 Hz. When the frequency is zero, the

impedance of the circuit is the sum of resistances: $R_0 + R_1 + R_2 = 1.8 \Omega$. Theoretically, at infinite frequency, the impedance of the circuit is its ohmic resistance: $R_0 = 0.5 \Omega$.

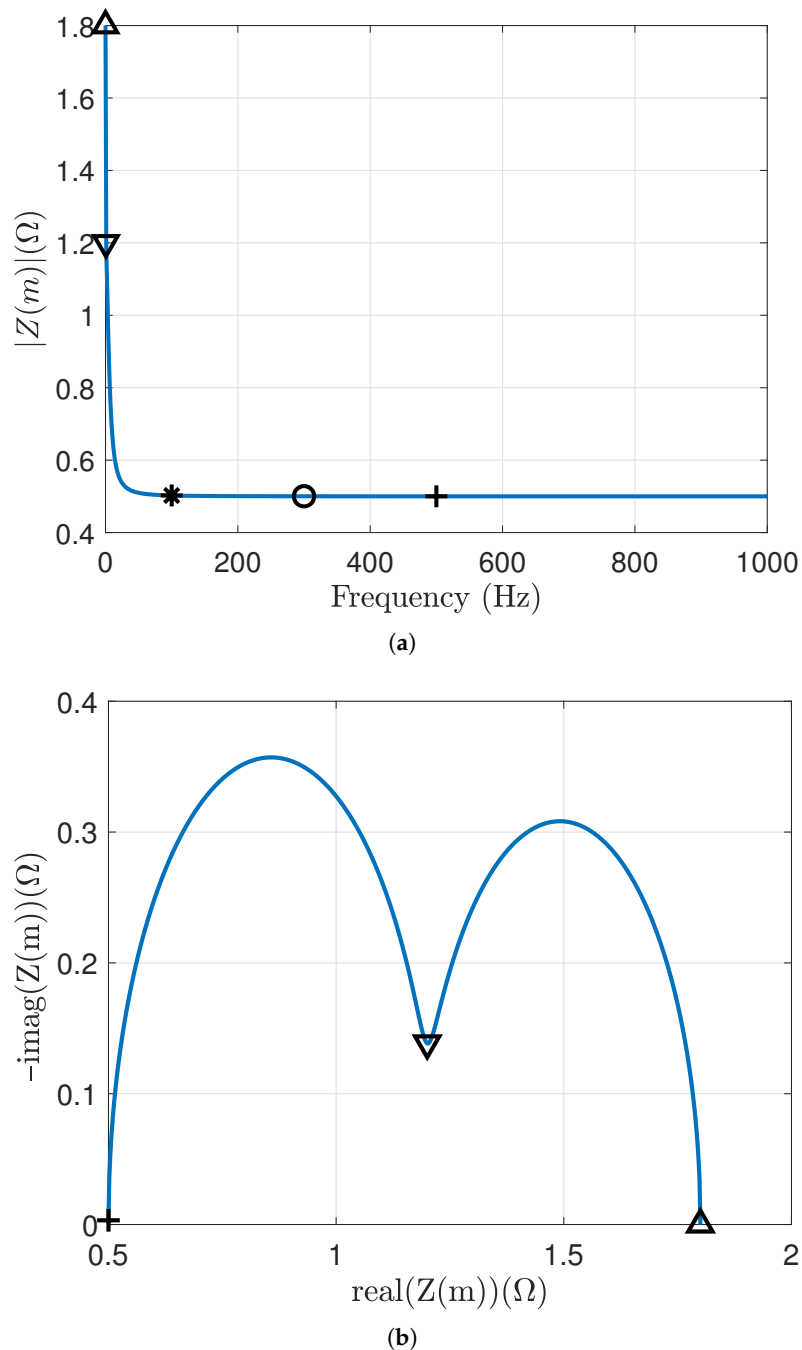


Figure 5. Frequency-domain response of the 2-RC circuit. (a) Theoretical impedance spectrum showing magnitude of impedance vs. frequencies. (b) Corresponding Nyquist plot showing real vs. imaginary impedance values.

The section of the plot in Figure 5b between markers Δ and ∇ indicates the low-frequency impedance response. It can be determined from Figure 5a that the corresponding low-frequency range varies between 0 Hz and ≈ 0.6 Hz. The section of the plot in Figure 5b between ∇ and $+$ is the high-frequency response of the circuit, with frequencies ranging from 0.6 Hz to 500 Hz.

The following demonstrations illustrate the effects of varying t_s and T_{on} , applying zero-padding, and changing the SNR levels on the Nyquist response.

5.1. Effect of Sampling Time

The impact of varying the sampling time, t_s , on the Nyquist plot is analyzed through simulations, and the results are shown in Figure 6. For each value of t_s , the pulse width, T_{on} , is set to $2t_s$ according to (34), while the rest period, T_{off} , is held constant at 40 s, chosen according to (37), where $10\tau_{max} = 30$ s. As t_s increases, the sampling frequency decreases, thereby limiting the maximum frequency captured to $f_s/2$, which narrows the observable frequency range.

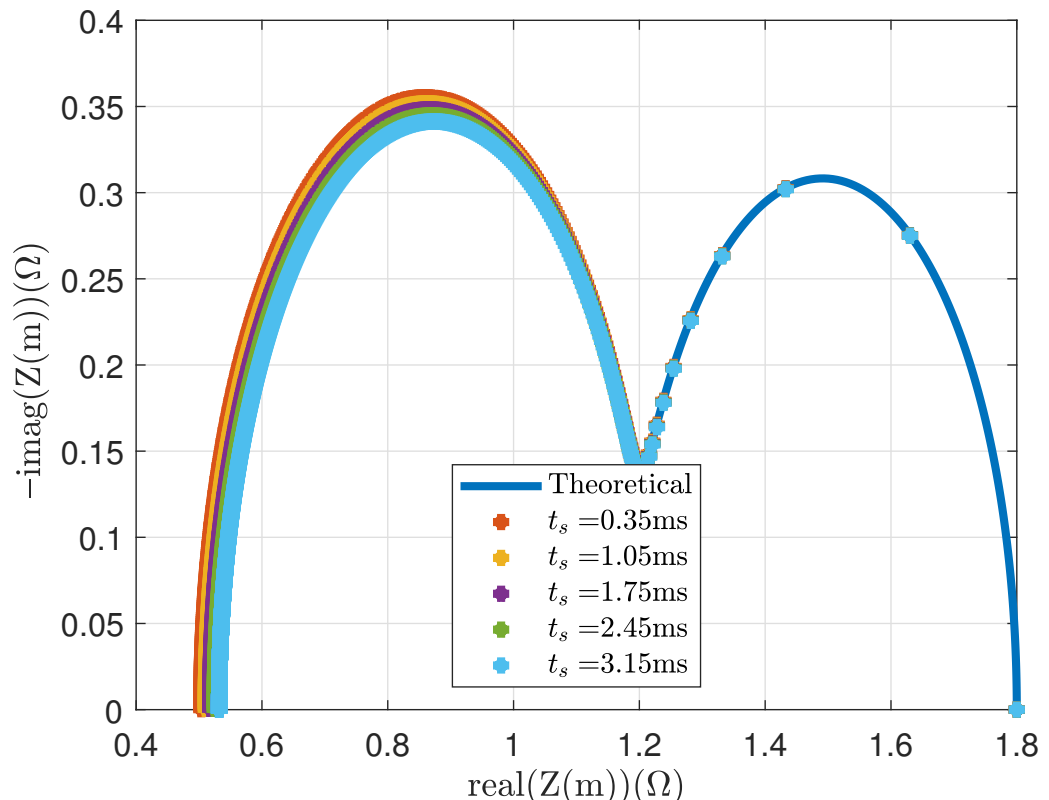


Figure 6. Effect of sampling time on the obtained impedance. As t_s decreases, the obtained impedance converges towards the reference spectrum.

The mean square error (MSE) in the simulated Nyquist plot for N_{runs} of Monte Carlo simulations is defined as

$$\text{MSE} = \frac{1}{N_{runs}} \sum_{r=1}^{N_{runs}} \text{MSE}_r \quad (40)$$

where

$$\text{MSE}_r = \frac{1}{N} \sum_{m=0}^{N-1} |Z_s(m) - Z_t(m)|^2 \quad (41)$$

MSE_r is the MSE for each run r , $Z_s(m)$ is the simulated Nyquist plot, and $Z_t(m)$ is the theoretical Nyquist plot.

The absolute relative percentage error in R_0 is defined as

$$\text{ARPE} = \left| \frac{\hat{R}_0 - R_0}{R_0} \right| * 100\% \quad (42)$$

where \hat{R}_0 is the observed high-frequency resistance from the Nyquist plot, and R_0 is its true value.

MSE (defined in (40)) and ARPE in R_0 (defined in (42)) for varying t_s values are shown in Figure 7a and 7b, respectively.

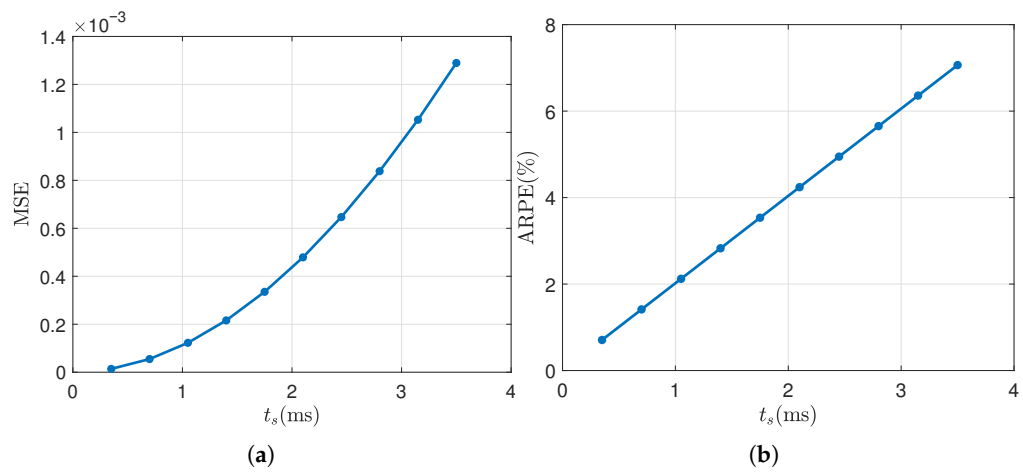


Figure 7. Effect of sampling time on accuracy. (a) MSE vs. t_s . (b) ARPE in R_0 vs. t_s .

5.2. Effect of T_{on}

The influence of different T_{on} values on the Nyquist plot is depicted in Figures 8 and 9. Pulse parameters are fixed at $t_s = 0.001$ s, and $T_{off} = 40$ s for this analysis. The excitation and response signal spectra are shown in Figure 8a and 8b, respectively. As T_{on} increases, the number of zero-crossings in the signals also increases.

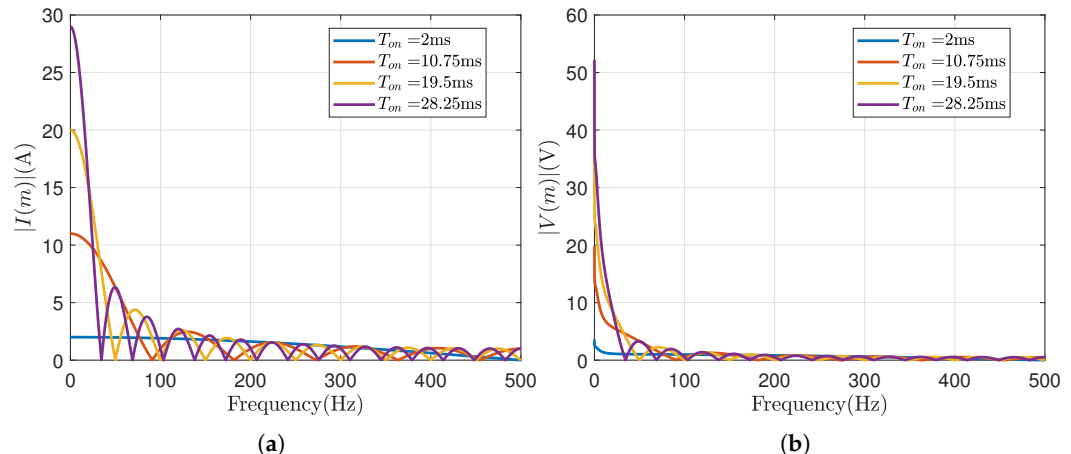


Figure 8. Effect of ON duration of pulse on the spectral content. (a) Excitation spectrum. (b) Response spectrum.

Figure 9 illustrates the corresponding Nyquist plot for varying T_{on} values. Although variations are apparent in the excitation and response spectra, the Nyquist plot remains largely unchanged across the T_{on} values considered. This lack of observable difference in the impedance results is attributed to the absence of noise in the analysis.

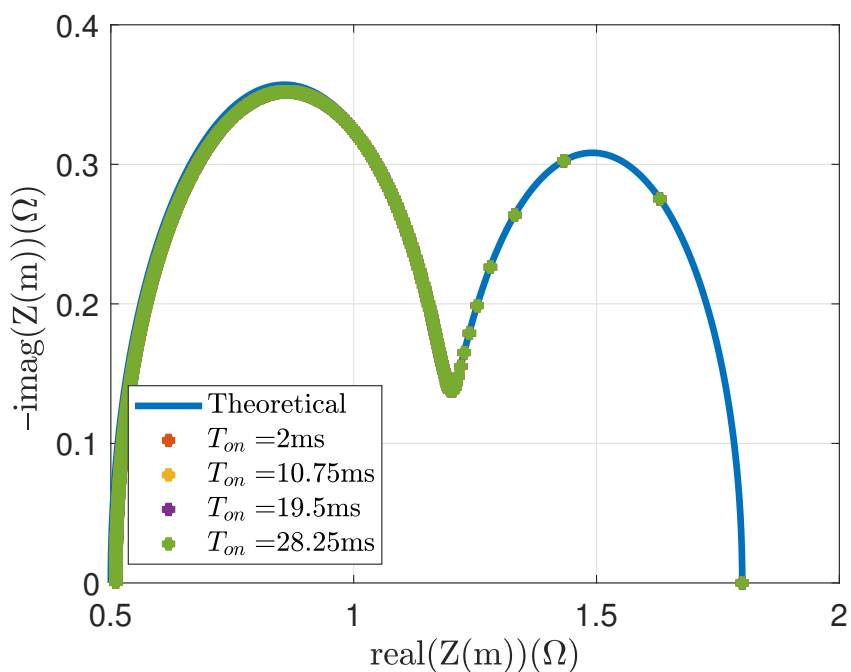


Figure 9. Effect of ON duration of pulse on the obtained impedance. Although increasing T_{on} alters the spectral content of the excitation and response signals, the resulting impedance spectra remain nearly identical in the noiseless case.

5.3. Effect of Zero-Padding

Figure 10a,b illustrate the impact of zero-padding the time-domain signal on the Nyquist plot. Figure 10b illustrates two cases of zero-padding, where zeros are appended to the original signal at lengths of 20 times and 10 times the original signal, respectively. It can be seen that zero-padding increases the number of frequency bins, thereby improving frequency resolution, especially in the lower frequency range. In this analysis, pulse parameters are maintained at $t_s = 0.001$ s, $T_{on} = 2t_s$, and $T_{off} = 40$ s.

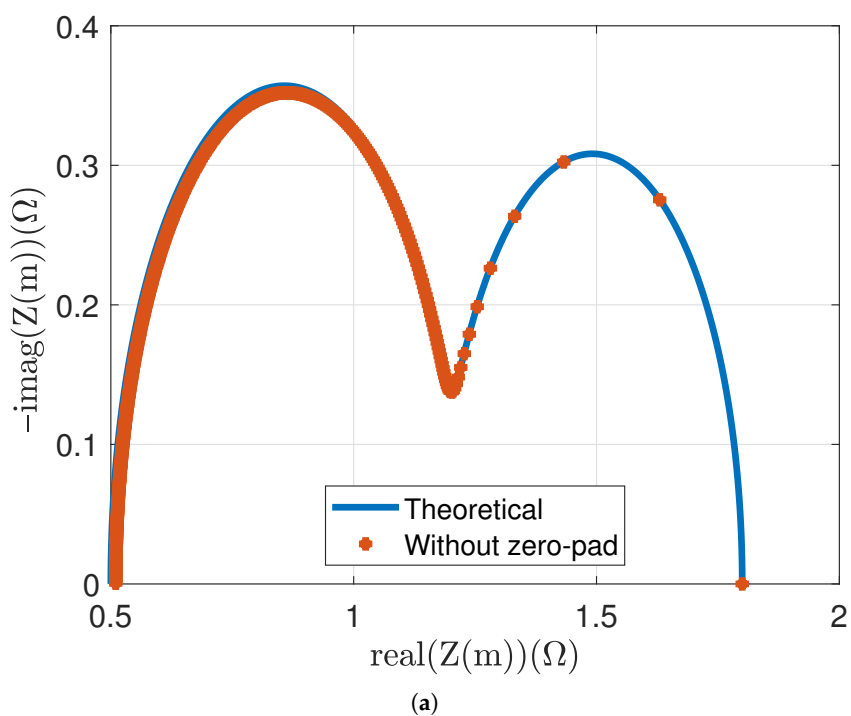


Figure 10. Cont.

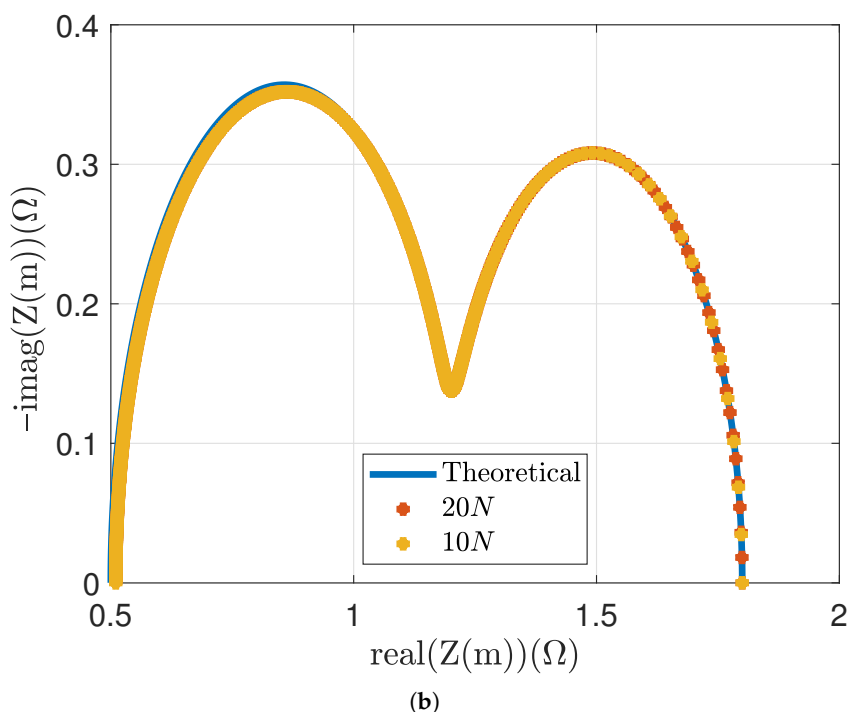


Figure 10. Effect of zero-padding on the obtained impedance. (a) Without zero-padding, the frequency resolution is limited by the signal length, causing sparse low-frequency data points. (b) Zero-padding increases the number of DFT frequency bins, improving resolution, especially in the low-frequency region, without extending the actual experiment duration.

5.4. Effect of SNR

This section analyzes the impact of varying SNR on the Nyquist plot. The results incorporate the proposed logarithmic frequency clustering and averaging approach, along with zero-padding to enhance frequency resolution.

The following summarizes the frequency clustering and the averaging method: Firstly, the uniformly spaced frequency points are grouped into logarithmically spaced bins, consistent with the frequency scales typically used in traditional EIS techniques. Within each bin, the noisy impedance measurements are averaged, resulting in a smoother impedance spectrum. Averaging on a logarithmic frequency scale reduces the effective number of measurements.

In this paper, we define the signal-to-noise ratio (SNR) of the excitation signal (current) as

$$\text{SNR}_e = 20 \log\left(\frac{I_0}{\sigma_i}\right) \quad (43)$$

where I_0 is the amplitude of the AC current excitation signal (or the amplitude of the step current pulse depending on the context) and σ_i is the standard deviation of the uncertainty in I_0 . The SNR of the measured battery voltage response varies depending on the SOC of the battery and its internal impedance. For simplicity, the SNR of the measured response is expressed as

$$\text{SNR}_m = 20 \log\left(\frac{1}{\sigma_v}\right) \quad (44)$$

where σ_v is the standard deviation of the voltage measurement noise. Figure 11a,b present two error metrics, MSE (defined in (40)) and ARPE in R_0 (defined in (42)), across varying T_{on} values. For this analysis, the SNR of the voltage measurement is varied between 45 dB

and 60 dB, while the current measurement is maintained at a constant SNR of 60 dB. Pulse parameters are fixed at $t_s = 0.001$ s and $T_{off} = 40$ s.

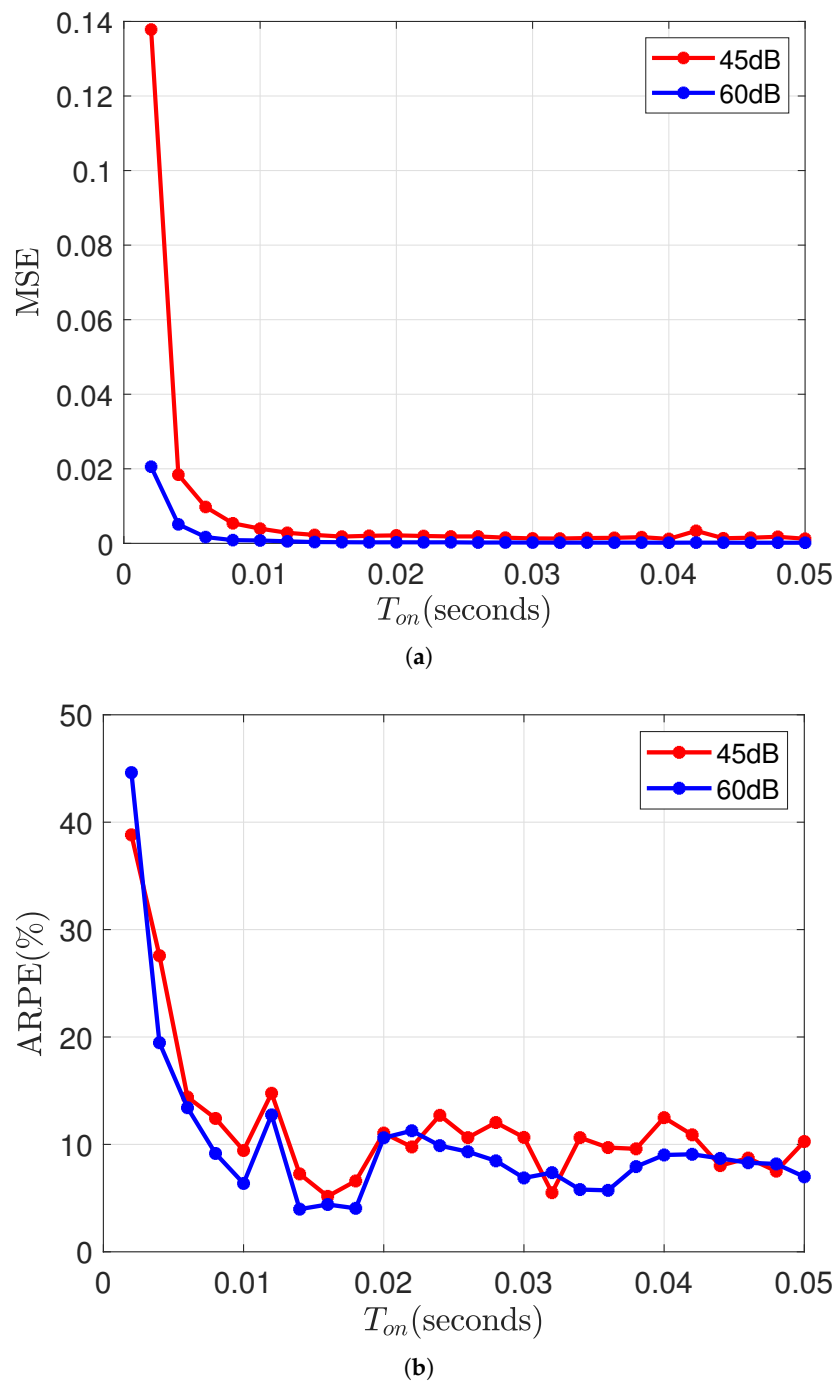


Figure 11. Effect of ON duration of pulse and SNR on accuracy. (a) MSE vs. T_{on} . (b) ARPE in R_0 vs. T_{on} .

It can be observed that when T_{on} is approximately equal to the minimum time constant, i.e., $T_{on} \approx \tau_{min}$, both the MSE and absolute percentage error reach a plateau.

6. Experimental Results

This section discusses the results of experiments performed on a designed 1-RC circuit whose parameters are known.

Pulse-EIS on the 1-RC Circuit

Figure 12 illustrates the designed 1-RC circuit connected to the Arbin battery cycler (LBT21084, Arbin Instruments, College Station, TX, USA), used to conduct experiments and collect data. The Arbin tester has 16 independently controlled channels, each with a voltage range of 0–5 V and a current range of ± 10 A.

The only time constant of the system is $\tau_{min} = \tau_{max} = 0.1$ s. The parameters of the excitation signal are determined considering the system's time constant and the recommendations outlined in the earlier discussion, i.e.,

$$t_s \leq \frac{1}{10} \tau_{min} \leq 0.01 = 0.005 \text{ s} \quad (45)$$

$$T_{on} = \tau_{min} = 0.1 \text{ s} \quad (46)$$

$$T_{off} \geq 10\tau_{max} \geq 1 \text{ s} \quad (47)$$

where T_{off} is chosen as ≈ 1.9 s and $T_{total} = 2$ s.

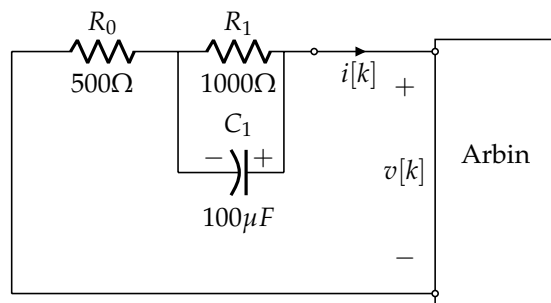


Figure 12. Experimental setup of the 1-RC circuit used for validation. The current excitation $i[k]$ is applied and the corresponding voltage response $v[k]$ is measured using the Arbin test system.

Figure 13 shows the excitation current signal (in blue) of amplitude ≈ 5 mA applied to the 1-RC circuit for an ON duration of 0.1 s, with a total duration of 2 s, and its voltage response (in red).

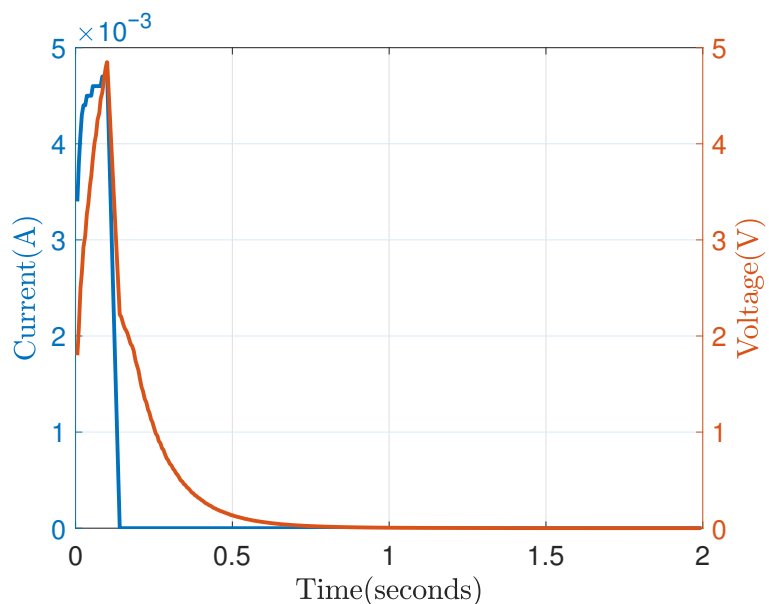


Figure 13. Measured current and voltage responses of the 1-RC circuit under pulse excitation. The current pulse (blue) produces a corresponding voltage transient (red) that decays exponentially, consistent with the first-order RC dynamics. These time-domain signals form the input–output data used for impedance estimation.

Figure 14a,b show the spectra of the excitation signal and voltage response obtained through the FFT.

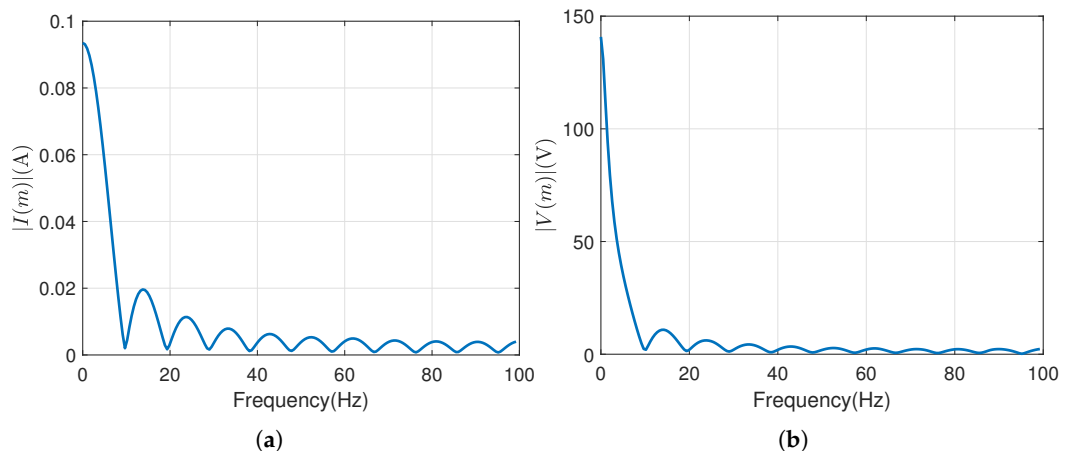


Figure 14. Frequency-domain spectra of the measured signals from the 1-RC circuit. (a) Magnitude spectrum of the excitation current. (b) Magnitude spectrum of the corresponding voltage response.

Using the proposed pulse signal, Figure 15a shows the obtained raw impedance data, and Figure 15b shows the zero-padded and log-cluster-averaged impedance spectrum.

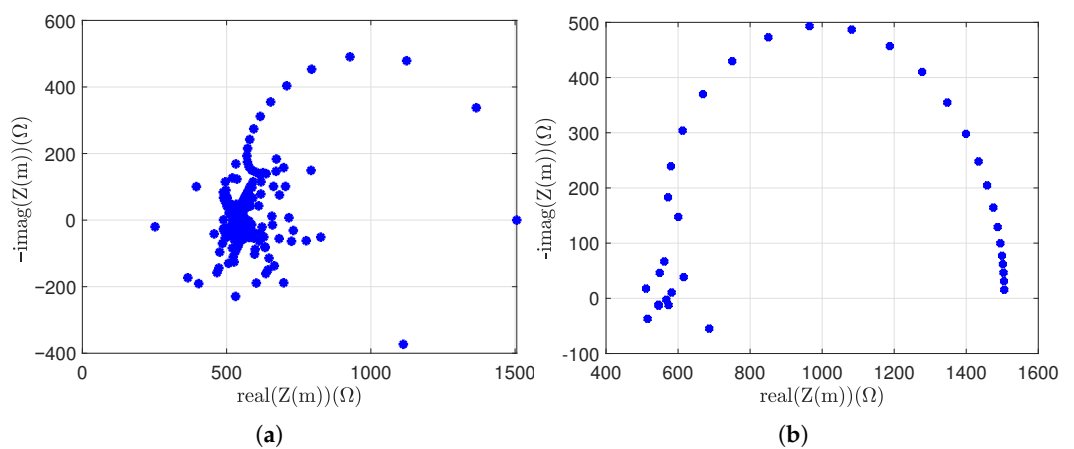


Figure 15. Pulse-EIS results for the 1-RC circuit. (a) Raw impedance data. (b) Processed impedance data after zero-padding and log-cluster-based averaging.

Figure 16 shows the pulse-EIS in comparison to the state-of-the-art EIS using sinusoidal signals and the theoretical plot. The state-of-the-art EIS response is obtained using the Gamry interface 5000P by exciting the RC circuit using sinusoidal signals of frequencies 0.01 Hz to 100 Hz.

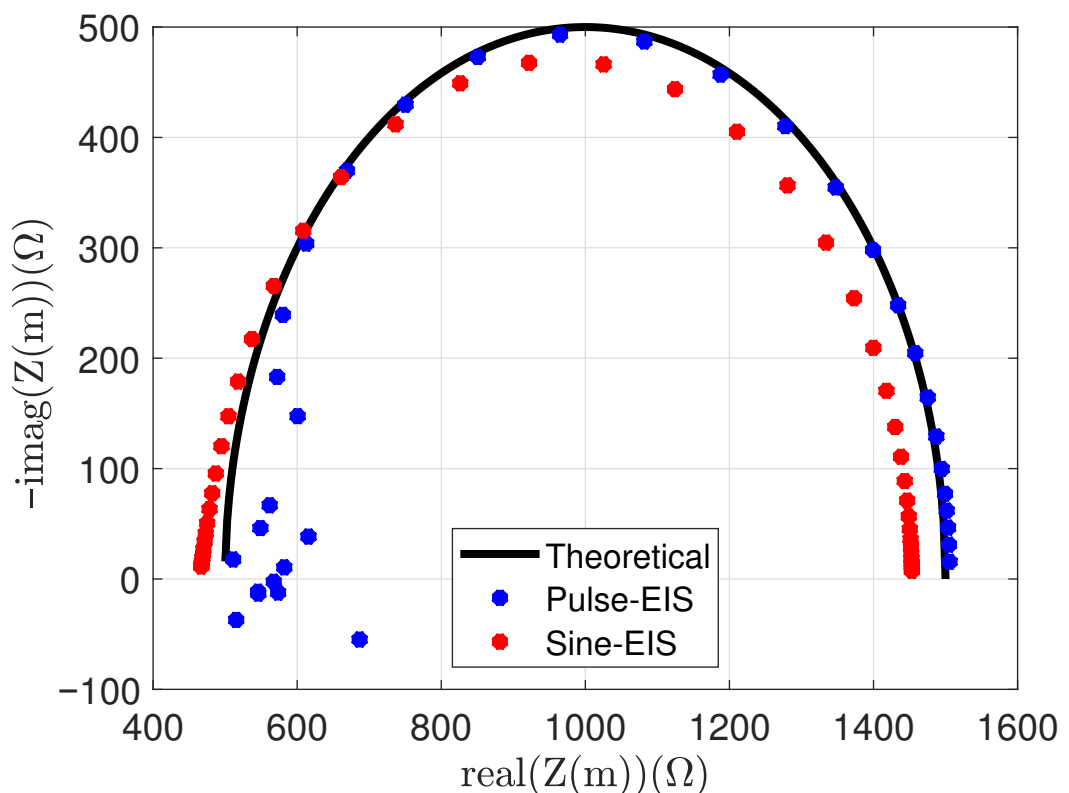


Figure 16. Comparison of the Nyquist impedance plots for the 1-RC circuit showing the theoretical impedance alongside results obtained using the proposed pulse-EIS and classical sine-EIS methods.

7. Conclusions

The key findings of this paper are summarized below:

1. There is a rule of thumb to selecting the sampling time: The sampling time, t_s , should be chosen to be less than at least one-tenth of the system's minimum time constant, i.e., $t_s \leq \frac{1}{10}\tau_{min}$.
2. There is a rule of thumb for the excitation pulse design: The pulse excitation signal comprises a non-zero portion lasting T_{on} and a zero portion lasting T_{off} . A general rule of thumb for selecting these durations is to set T_{on} approximately equal to the minimum time constant, i.e., $T_{on} \approx \tau_{min}$ of the system, and T_{off} to approximately ten times the maximum time constant, i.e., $T_{off} \geq 10\tau_{max}$.
3. Noise can be reduced through averaging: This paper demonstrates that the measurement noise in both voltage and current signals retains its zero-mean property after applying the discrete Fourier transform, enabling effective noise reduction through averaging.
4. Zero-padding improves resolution: When a pulse excitation signal is used, the resulting responses are unevenly distributed across the frequency domain, with a higher concentration appearing in the high-frequency region. To improve resolution in the low-frequency range, zero-padding is applied. While zero-padding also increases resolution in the high-frequency region, responses from closely spaced frequencies can be grouped and averaged to reduce noise. This approach leads to a more balanced spectral distribution.

Author Contributions: Conceptualization, B.B. and K.R.P.; methodology, B.B. and S.S.; software, S.S.; validation, S.S.; formal analysis, S.S.; data curation, S.S.; writing—original draft preparation, S.S.; writing—review and editing, B.B., K.R.P., and S.S.; visualization, S.S.; supervision, B.B.; project administration, B.B.; funding acquisition, B.B. All authors have read and agreed to the published version of the manuscript.

Funding: This research was funded by the Natural Sciences and Engineering Research Council of Canada (NSERC) grant number RGPIN-2024-04557.

Data Availability Statement: The original contributions presented in the study are included in the article, further inquiries can be directed to the corresponding author.

Conflicts of Interest: The authors declare no conflicts of interest. The funders had no role in the design of the study; in the collection, analyses, or interpretation of data; in the writing of the manuscript; or in the decision to publish the results.

Appendix A. DFT of Excitation Signal

For the signal defined in (1), the DFT is

$$I(m) = \sum_{k=0}^{K-1} -ae^{-jm(\frac{2\pi}{N})^k}, \quad m = 0, 1, \dots, N-1 \quad (\text{A1})$$

Denote $b = m\frac{2\pi}{N}$, and by the sum of geometric progression, (A1) is

$$I(m) = -a \left(\frac{(e^{-jb})^K - 1}{e^{-jb} - 1} \right) \quad (\text{A2})$$

$$= -a \frac{(e^{-jb})^{K/2}}{e^{-jb/2}} \left(\frac{(e^{-jb})^{K/2} - (e^{jb})^{K/2}}{e^{-jb/2} - e^{jb/2}} \right) \quad (\text{A3})$$

$$= -ae^{-j\frac{b}{2}(K-1)} \frac{\sin(bK/2)}{\sin(b/2)} \quad (\text{A4})$$

$$= -ae^{-jm\frac{\pi}{N}(K-1)} \left(\frac{\sin(\frac{mK\pi}{N})}{\sin(\frac{m\pi}{N})} \right), \quad m = 1, \dots, N-1 \quad (\text{A5})$$

For $m = 0$, $I(0) = -aK$.

Appendix B. Mean of the Transformed Voltage and Current Noise

The DFT of the voltage noise is shown in (10). Considering voltage noise at the m^{th} frequency bin to be denoted by $N_v(m)$, we have

$$N_v(m) = \mathbf{a}^T \mathbf{n}_v = \mathbf{a}_r^T \mathbf{n}_v + j\mathbf{a}_i^T \mathbf{n}_v \quad (\text{A6})$$

$$= N_{vr}(m) + jN_{vi}(m) \quad (\text{A7})$$

The mean of the transformed voltage noise, given \mathbf{n}_v is assumed to be zero-mean noise, is

$$\mathbb{E}[N_{vr}(m)] = \mathbb{E}[\mathbf{a}_r^T \mathbf{n}_v] = 0 \quad (\text{A8})$$

$$\mathbb{E}[N_{vi}(m)] = \mathbb{E}[\mathbf{a}_i^T \mathbf{n}_v] = 0 \quad (\text{A9})$$

Similarly, it can be shown that the zero-mean property is preserved in the transformed current noise.

References

- Chen, H.; Bai, J.; Wu, Z.; Song, Z.; Zuo, B.; Fu, C.; Zhang, Y.; Wang, L. Rapid impedance measurement of Lithium-Ion batteries under pulse ex-citation and analysis of impedance characteristics of the regularization distributed relaxation time. *Batteries* **2025**, *11*, 91. [[CrossRef](#)]
- Nunes, H.; Martinho, J.; Fermeiro, J.; Pombo, J.; Mariano, S.; do Rosário Calado, M. Impedance analysis and parameter estimation of lithium-ion batteries using the eis technique. *IEEE Trans. Ind. Appl.* **2024**, *60*, 5048–5060. [[CrossRef](#)]

3. Meddings, N.; Heinrich, M.; Overney, F.; Lee, J.S.; Ruiz, V.; Napolitano, E.; Seitz, S.; Hinds, G.; Raccichini, R.; Gaberšček, M.; et al. Application of electrochemical impedance spectroscopy to commercial Li-ion cells: A review. *J. Power Sources* **2020**, *480*, 228742. [[CrossRef](#)]
4. Messing, M.; Shoa, T.; Ahmed, R.; Habibi, S. Battery SoC estimation from EIS using neural nets. In Proceedings of the 2020 IEEE Transportation Electrification Conference & Expo (ITEC), Chicago, IL, USA, 23–26 June 2020; IEEE: Piscataway, NJ, USA, 2020; pp. 588–593.
5. Bourelly, C.; Vitelli, M.; Milano, F.; Molinara, M.; Fontanella, F.; Ferrigno, L. Eis-based soc estimation: A novel measurement method for optimizing accuracy and measurement time. *IEEE Access* **2023**, *11*, 91472–91484. [[CrossRef](#)]
6. Li, C.; Yang, L.; Li, Q.; Zhang, Q.; Zhou, Z.; Meng, Y.; Zhao, X.; Wang, L.; Zhang, S.; Li, Y.; et al. SOH estimation method for lithium-ion batteries based on an improved equivalent circuit model via electrochemical impedance spectroscopy. *J. Energy Storage* **2024**, *86*, 111167. [[CrossRef](#)]
7. Zhou, Z.; Li, Y.; Wang, Q.G.; Yu, J. Health indicators identification of lithium-ion battery from electrochemical impedance spectroscopy using geometric analysis. *IEEE Trans. Instrum. Meas.* **2023**, *72*, 1501709. [[CrossRef](#)]
8. Teliz, E.; Zinola, C.F.; Díaz, V. Identification and quantification of ageing mechanisms in Li-ion batteries by Electrochemical impedance spectroscopy. *Electrochim. Acta* **2022**, *426*, 140801. [[CrossRef](#)]
9. Fu, Y.; Xu, J.; Shi, M.; Mei, X. A fast impedance calculation-based battery state-of-health estimation method. *IEEE Trans. Ind. Electron.* **2021**, *69*, 7019–7028. [[CrossRef](#)]
10. Li, A.G.; West, A.C.; Preindl, M. Characterizing degradation in lithium-ion batteries with pulsing. *J. Power Sources* **2023**, *580*, 233328. [[CrossRef](#)]
11. Wu, Y.; Sundaresan, S.; Balasingam, B. Battery parameter analysis through electrochemical impedance spectroscopy at different state of charge levels. *J. Low Power Electron. Appl.* **2023**, *13*, 29. [[CrossRef](#)]
12. Abaspour, M.; Pattipati, K.R.; Shahrrava, B.; Balasingam, B. Robust approach to battery equivalent-circuit-model parameter extraction using electrochemical impedance spectroscopy. *Energies* **2022**, *15*, 9251. [[CrossRef](#)]
13. Srinivasan, R.; Fasmin, F. *An Introduction to Electrochemical Impedance Spectroscopy*; CRC Press: Boca Raton, FL, USA, 2021.
14. Pérez, G.; Gandiaga, I.; Garmendia, M.; Reynaud, J.; Viscarret, U. Modelling of Li-ion batteries dynamics using impedance spectroscopy and pulse fitting: EVs application. In Proceedings of the 2013 World Electric Vehicle Symposium and Exhibition (EVS27), Barcelona, Spain, 17–20 November 2013; IEEE:Piscataway, NJ, USA, 2013; pp. 1–9.
15. Schmidt, J.P.; Ivers-Tiffée, E. Pulse-fitting—A novel method for the evaluation of pulse measurements, demonstrated for the low frequency behavior of lithium-ion cells. *J. Power Sources* **2016**, *315*, 316–323. [[CrossRef](#)]
16. Kollmeyer, P.; Hackl, A.; Emadi, A. Li-ion battery model performance for automotive drive cycles with current pulse and EIS parameterization. In Proceedings of the 2017 IEEE Transportation Electrification Conference and Expo (ITEC), Chicago, IL, USA, 22–24 June 2017; IEEE: Piscataway, NJ, USA, 2017; pp. 486–492.
17. Tang, X.; Lai, X.; Liu, Q.; Zheng, Y.; Zhou, Y.; Ma, Y.; Gao, F. Predicting battery impedance spectra from 10-second pulse tests under 10 Hz sampling rate. *IScience* **2023**, *26*, 106821. [[CrossRef](#)]
18. Li, A.G.; Fahmy, Y.A.; Wu, M.M.; Preindl, M. Fast time-domain impedance spectroscopy of lithium-ion batteries using pulse perturbation. In Proceedings of the 2022 IEEE Transportation Electrification Conference & Expo (ITEC), Anaheim, CA, USA, 15–17 June 2022; IEEE: Piscataway, NJ, USA, 2022; pp. 155–160.
19. Wang, L.; Song, Z.; Zhu, L.; Jiang, J. Fast electrochemical impedance spectroscopy of lithium-ion batteries based on the large square wave excitation signal. *IScience* **2023**, *26*, 106463. [[CrossRef](#)] [[PubMed](#)]
20. Boškoski, P.; Debenjak, A.; Mileva Boshkoska, B.; Boškoski, P.; Debenjak, A.; Mileva Boshkoska, B. *Fast Electrochemical Impedance Spectroscopy*; Springer: Berlin/Heidelberg, Germany, 2017.
21. Gabrielli, C.; Huet, F.; Keddam, M.; Lizée, J. Measurement time versus accuracy trade-off analyzed for electrochemical impedance measurements by means of sine, white noise and step signals. *J. Electroanal. Chem. Interfacial Electrochem.* **1982**, *138*, 201–208. [[CrossRef](#)]
22. Duhamel, P.; Vetterli, M. Fast Fourier transforms: A tutorial review and a state of the art. *Signal Process.* **1990**, *19*, 259–299. [[CrossRef](#)]
23. Takano, K.; Nozaki, K.; Saito, Y.; Kato, K.; Negishi, A. Impedance Spectroscopy by Voltage-Step Chronoamperometry Using the Laplace Transform Method in a Lithium-Ion Battery. *J. Electrochem. Soc.* **2000**, *147*, 922. [[CrossRef](#)]
24. Onda, K.; Nakayama, M.; Fukuda, K.; Wakahara, K.; Araki, T. Cell impedance measurement by Laplace transformation of charge or discharge current–voltage. *J. Electrochem. Soc.* **2006**, *153*, A1012. [[CrossRef](#)]
25. Li, T.; Wang, D.; Wang, H. New method for acquisition of impedance spectra from charge/discharge curves of lithium-ion batteries. *J. Power Sources* **2022**, *535*, 231483. [[CrossRef](#)]
26. Wang, X.; Kou, Y.; Wang, B.; Jiang, Z.; Wei, X.; Dai, H. Fast Calculation of Broadband Battery Impedance Spectra Based on S Transform of Step Disturbance and Response. *IEEE Trans. Transp. Electrif.* **2022**, *8*, 3659–3672. [[CrossRef](#)]

27. Li, W.; Huang, Q.A.; Yang, C.; Chen, J.; Tang, Z.; Zhang, F.; Li, A.; Zhang, L.; Zhang, J. A fast measurement of Warburg-like impedance spectra with Morlet wavelet transform for electrochemical energy devices. *Electrochim. Acta* **2019**, *322*, 134760. [[CrossRef](#)]
28. Hoshi, Y.; Yakabe, N.; Isobe, K.; Saito, T.; Shitanda, I.; Itagaki, M. Wavelet transformation to determine impedance spectra of lithium-ion rechargeable battery. *J. Power Sources* **2016**, *315*, 351–358. [[CrossRef](#)]
29. Itagaki, M.; Ueno, M.; Hoshi, Y.; Shitanda, I. Simultaneous determination of electrochemical impedance of lithium-ion rechargeable batteries with measurement of charge-discharge curves by wavelet transformation. *Electrochim. Acta* **2017**, *235*, 384–389. [[CrossRef](#)]
30. Lohmann, N.; Weßkamp, P.; Hauffmann, P.; Melbert, J.; Musch, T. Electrochemical impedance spectroscopy for lithium-ion cells: Test equipment and procedures for aging and fast characterization in time and frequency domain. *J. Power Sources* **2015**, *273*, 613–623. [[CrossRef](#)]
31. Cicioni, G.; De Angelis, A.; Janeiro, F.M.; Ramos, P.M.; Carbone, P. Battery impedance spectroscopy embedded measurement system. *Batteries* **2023**, *9*, 577. [[CrossRef](#)]
32. Fan, C.; Tian, X.; Gu, C. Perturbation-based battery impedance characterization methods: From the laboratory to practical implementation. *Batteries* **2024**, *10*, 414. [[CrossRef](#)]
33. Guha, A.; Patra, A. Online estimation of the electrochemical impedance spectrum and remaining useful life of lithium-ion batteries. *IEEE Trans. Instrum. Meas.* **2018**, *67*, 1836–1849. [[CrossRef](#)]
34. Qahouq, J.A.A.; Xia, Z. Single-Perturbation-Cycle Online Battery Impedance Spectrum Measurement Method With Closed-Loop Control of Power Converter. *IEEE Trans. Ind. Electron.* **2017**, *64*, 7019–7029. [[CrossRef](#)]
35. Crescentini, M.; De Angelis, A.; Ramilli, R.; De Angelis, G.; Tartagni, M.; Moschitta, A.; Traverso, P.A.; Carbone, P. Online EIS and Diagnostics on Lithium-Ion Batteries by Means of Low-Power Integrated Sensing and Parametric Modeling. *IEEE Trans. Instrum. Meas.* **2021**, *70*, 2001711. [[CrossRef](#)]
36. Zhu, J.; Lai, X.; Zhu, Z.; Ke, P.; Zheng, Y.; Tang, X.; Li, X.; Yuan, Y.; Chong, H.; Yan, C.; et al. Online generation of full-frequency electrochemical impedance spectra for Lithium-ion batteries using early-stage partial relaxation voltage curve. *eTransportation* **2025**, *26*, 100482. [[CrossRef](#)]
37. Ovejas, V.J.; Cuadras, A. Impedance characterization of an LCO-NMC/graphite cell: Ohmic conduction, SEI transport and charge-transfer phenomenon. *Batteries* **2018**, *4*, 43. [[CrossRef](#)]
38. Bakierska, M.; Świętosławski, M.; Dziembaj, R.; Molenda, M. Nature of the electrochemical properties of sulphur substituted LiMn_2O_4 spinel cathode material studied by electrochemical impedance spectroscopy. *Materials* **2016**, *9*, 696. [[CrossRef](#)]
39. Li, Y.D.; Zhao, S.X.; Nan, C.W.; Li, B.H. Electrochemical performance of SiO_2 -coated LiFePO_4 cathode materials for lithium ion battery. *J. Alloys Compd.* **2011**, *509*, 957–960. [[CrossRef](#)]
40. Eliseeva, S.; Apraksin, R.; Tolstopiatova, E.; Kondratiev, V. Electrochemical impedance spectroscopy characterization of LiFePO_4 cathode material with carboxymethylcellulose and poly-3,4-ethylendioxythiophene/polystyrene sulfonate. *Electrochim. Acta* **2017**, *227*, 357–366. [[CrossRef](#)]
41. Balasingam, B. *Robust Battery Management System Design with MATLAB*; Artech House: Washington, DC, USA, 2023.
42. Kuo, B.C. *Automatic Control Systems*; Prentice Hall PTR: Upper Saddle River, NJ, USA, 1987.
43. Lu, Y.; Zhao, C.Z.; Huang, J.Q.; Zhang, Q. The timescale identification decoupling complicated kinetic processes in lithium batteries. *Joule* **2022**, *6*, 1172–1198. [[CrossRef](#)]
44. Sundaresan, S.; Pattipati, K.; Balasingam, B. Fast Electrochemical Impedance Spectroscopy for Battery Testing. In Proceedings of the 2025 IEEE 34th International Symposium on Industrial Electronics (ISIE), Toronto, ON, Canada, 20–23 June 2025; pp. 1–6. [[CrossRef](#)]

Disclaimer/Publisher’s Note: The statements, opinions and data contained in all publications are solely those of the individual author(s) and contributor(s) and not of MDPI and/or the editor(s). MDPI and/or the editor(s) disclaim responsibility for any injury to people or property resulting from any ideas, methods, instructions or products referred to in the content.